Research Article

Synthesis and High Electrocatalytic Performance of Hexagram Shaped Gold Particles Having an Open Surface Structure with Kinks

Qingning Jiang[§], Zhiyuan Jiang[§], Lei Zhang, Haixin Lin, Ning Yang, Huan Li, Deyu Liu, Zhaoxiong Xie (✉), and Zhongqun Tian

State Key Laboratory for Physical Chemistry of Solid Surfaces, Department of Chemistry, College of Chemistry and Chemical Engineering, Xiamen University, Xiamen 361005, China

ABSTRACT

Hexagram shaped gold particles and their analogues enclosed by high index facets with kinks have been successfully synthesized by reducing $HAuCl_4$ with ascorbic acid (AA) in the presence of poly(diallyldimethylammonium chloride) at room temperature. By using electron microscopy, the surfaces of the hexagram shaped Au particle were found to be {541} planes, which contain high-density steps and kinks. In addition, it was found that hexagonal shield-like and other kind of particles present in the product were analogues of the hexagram shaped Au particles structure, in that they had the same surface structure. In order to confirm the surface structure of all the prepared particles, surface structure sensitive underpotential deposition of Pb was carried out, and the cyclic voltammetric profile was in accordance with the proposed {541} surface. Finally, structure–property relationships of the Au hexagrams were experimentally analyzed by employing the electrocatalytic oxidation of AA as a probe reaction. The electrocatalytic reactions of gold cubes with low-index {100} facets and gold trioctahedra with {221} facets were studied as references. The experimental results showed that the hexagram shaped Au particles and their analogues with exposed {541} facets have the highest catalytic activity among the three kinds of gold particles, owing to the high density of kink atoms. This study should motivate us to further explore methods for the preparation of other well-defined polyhedral metal nanocrystals enclosed by high index surfaces.

1. Introduction

Fundamental studies of single-crystal surfaces have indicated that different facets of a single crystal may exhibit different physical and chemical properties [1–4]. Therefore, the surface-controlled growth of nanocrystals (NCs) may tailor the properties of crystalline materials, and have potential applications in various fields such as catalysis [5–13]. The recent construction of NCs with high-surface-energy facets represents a

---

Address correspondence to zxxie@xmu.edu.cn
[§] These authors contributed equally to this work.

new trend in advanced functional materials because they usually exhibit better performances than conventional NCs. For example, TiO_2 NCs with dominant high-surface-energy {001} facets showed excellent photocatalytic properties [14–16], and Co_3O_4 nanorods with exposed {110} facets could catalyze CO oxidation at low temperature in feed gases containing large amounts of H_2O [17].

For noble metal NCs, high index facets represent high-surface-energy facets, which have high density atomic steps, ledges, kinks, and dangling bonds [18, 19]. However, noble metal NCs are usually enclosed by low index facets because of their relatively low surface energy and growth rate [20–22]. The pioneering work in the preparation of NCs with high index facets was carried out by Sun et al. who used a special electrochemical method to prepare tetrahexahedral Pt NCs enclosed by 24 {hk0} high index facets [23]. Subsequently, trapezohedral Pt NCs with 24 {hkk} facets, concave hexoctahedral Pt NCs with 48 {hkl} facets, and multiple twinned Pt nanorods with {hk0} facets were also synthesized by the electrochemical method [24].

In addition to electrochemical methods, the use of conventional solution-based methods for the growth of noble metal NCs with high index facets has also been reported by a few groups, including our own. For example, trioctahedral gold (Au) NCs enclosed by 24 high index ({hhl} facets such as {221}) [25], elongated tetrahexahedral Au NCs with exposed {730} facets [26], star-shaped Au NCs with {331} facets [27], concave cubic gold NCs enclosed by 24 {720} facets [28], concave trisoctahedral Au NCs bounded by {hhl} facets [29], tetrahexahedral Au NCs with exposed {520} facets [30] and tetrahexahedral Au NCs bound to {210} facets [31] have been reported. To date, however, all the reported Au NCs enclosed by high index facets involve {hhl} or {hk0} facets, which consist of low index terraces and steps. Metal NCs with higher index facets (denoted as {hkl}) contain kinks that have much higher surface energy and disappear more rapidly during crystal growth, and therefore, it is much more difficult to obtain metal particles having high index facets with kinks via solution-based crystal growth. Our work aims to achieve this goal and demonstrate the importance of structure–functionality relationships.

In this study, we report a relatively new and facile colloidal process for the controllable synthesis of hexagram shaped Au particles and their analogues by using a polyelectrolyte as the stabilizer rather than a traditional stabilizing agent. Combining the results of electron microscopy and surface sensitive electrochemical analysis, we showed that the as-prepared particles are enclosed by high index {hkl} facets (such as {541} facets) with kinks. This is the first report of Au particles having a high index surface with kinks. In addition, it has been demonstrated that the as-prepared Au particles exhibit excellent electrocatalytic activity.

2. Experimental

2.1 Reagents

Poly(diallyldimethylammonium chloride) (PDDA, 35 wt% in water, M_w <100 000) was purchased from Sigma-Aldrich. $HAuCl_4 \cdot 4H_2O$ (99.9%) and ascorbic acid (AA), were purchased from Sinopharm Chemical Reagent Co. Ltd. (Shanghai, China). The water used in all experiments was ultrapure (>18.0 MΩ/cm). All reagents were used as purchased without further purification.

2.2 Synthesis of hexagram shaped gold particles and their analogues

0.25 mL of $HAuCl_4$ (24.28 mmol/L) was added into a 5 mL portion of as-purchased PDDA solution in water and stirred for 10 min at room temperature. Then a freshly prepared aqueous solution of AA (0.8 mL, 0.1 mol/L) was quickly added to the solution with vigorous stirring. The solution became colorless and transparent in several seconds. With continuous shaking, the solution gradually became light red-orange in color. The solution was then centrifuged several times at 7000 rpm to remove excess reactants and PDDA.

2.3 Structural characterization and electrochemical measurements

The as-prepared Au NCs were characterized by scanning electron microscopy (SEM, Hitachi S-4800, operated at 10 kV), and transmission electron microscopy (TEM, FEI Tecnai-F30 FEG, operated at 300 kV).

Cyclic voltammetry (CV) measurements were carried out in a standard three-electrode cell at room temperature. The reference electrode was a saturated calomel electrode (SCE), and the counter electrode was Pt foil. Before being used as a support electrode, a glassy carbon (GC) electrode ($\phi = 3$ mm) was polished successively with alumina powder (Buehler Ltd., Lake Bluff, IL) from 3 μm down to 0.05 μm to achieve a mirror finish surface, followed by ultrasonication in Milli-Q water for 3 min after each polishing step. It was then cleaned in 0.1 mol/L H_2SO_4 by scanning the potential between –0.25 V and +1.25 V at 400 mV/s for 10 min before use. Then, a drop of the prepared gold sol was dripped onto the surface of the GCE and dried at room temperature. The surface of the electrode was covered by an obvious and uniform layer of the NCs. The electrolytes were 0.1 mol/L NaOH + 10^{-3} mol/L $Pb(NO_3)_2$ for the Pb underpotential deposition (UPD), and 10 mmol/L AA in 0.1 mol/L phosphate buffered solution (PBS) (the pH value was about 7.04) for the AA oxidation. The solutions were thoroughly purged with N_2 before each experiment.

3. Results and discussion

3.1 Structural characterization of hexagram shaped gold particles and their analogues

The hexagram shaped Au particles and their analogues were successfully synthesized via a simple wet chemical method using $HAuCl_4 \cdot 4H_2O$ as precursor, AA as reactant and PDDA solution as the solvent. The morphologies of the products were investigated by SEM. As shown in Fig. 1(a), over 35% of the products exhibited regular six-fold symmetry and displayed a strikingly beautiful hexagram shaped crystallite geometry. The size was in the range of 400 nm to 800 nm. To elucidate the detailed morphology of the hexagram particles, the SEM specimen stage was rotated and imaged with different tilt angles. It was found that the Au hexagram was a well-shaped polyhedron, whose outline varied from hexagram to rhombus (Fig. 1(b)). From the SEM images, the basic geometrical angles of the hexagram shaped Au particles can be deduced. The hexagram shaped crystals have 24 smooth trigonal facets. The angle between the


(a)

(b)
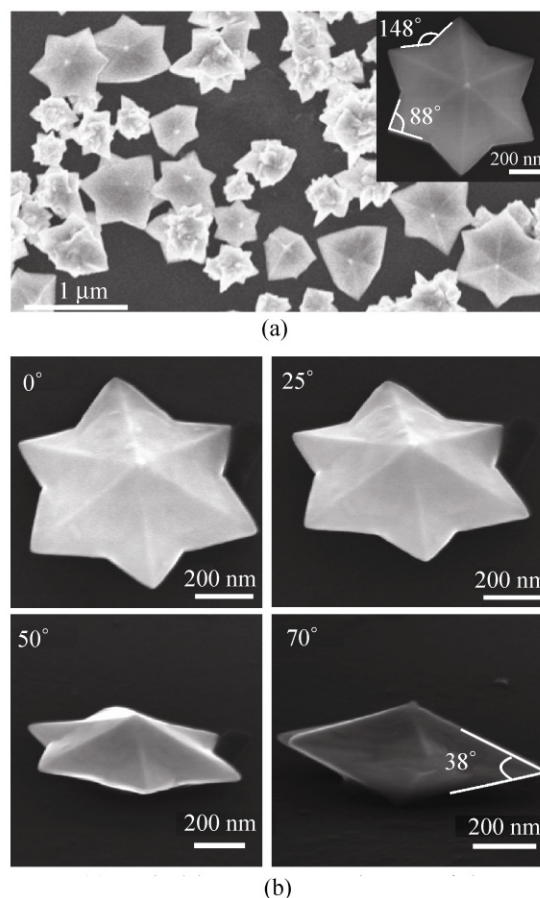
Figure 1 (a) Typical large-area SEM images of the as-prepared Au particles. Inset: high-magnification SEM image of a single hexagram shaped Au particle. (b) High-magnification SEM images of a hexagram shaped Au particle taken from different angles of the sample stage (0°, 25°, 50°, and 70°)

two salient edges of the hexagram shaped gold crystals is about 88°, the angle of the concave edges is about 148° (inset of Fig. 1(a)), and the angle between the edges of the upper and under surfaces is about 38° (Fig. 1(b)).

Although Au nanoparticles with branched hexagram shapes have been synthesized [20, 32], to the best of our knowledge, hexagram shaped Au crystals surrounded by 24 trigonal facets have not been reported previously. The structural features of the as-prepared hexagram particles were then further revealed by TEM images and selected area electron diffraction (SAED) patterns.

Figure 2(a) shows a TEM image of an individual hexagram with the same hexagonal star outline observed in the SEM images. The corresponding SAED patterns (Fig. 2(b)) were recorded by directing the

electron beam onto the whole individual Au crystal, and can be indexed as the diffractions of the [1$\bar{1}$1] zone axis. The diagonal of the hexagram can be determined to be the [112] direction according to the TEM observations, as marked by an arrow in Fig. 2(a). In addition, by carefully calibrating the SAED pattern, it can be found that the closest and the strongest reflections are not normal {220} Bragg reflections, but the formally forbidden 1/3{422} reflections. Figure 2(c) shows a high resolution TEM (HRTEM) image recorded from the region enclosed by a square in Fig. 2(a). The lattice spacing is 0.25 nm, triple that of the {422} lattice spacing of the face-centered cubic (fcc) Au crystal, agreeing well with the appearance of 1/3{422} diffractions in Fig. 2(b). HRTEM images of different part of this hexagram exhibit the same structural feature (Fig. S-1 in the Electronic Supplementary Material (ESM)). Au is an fcc metal. The closest strong reflections to the direct beam are the six allowed {220} Bragg reflections, and the next closest strong reflections are the six allowed {422} Bragg reflections. A number of models, such as a flat thin plates, surface reconstruction, twin structures and stacking faults, can be used to explain the occurrence of forbidden 1/3{422} reflections [33–36]. In the present case, flat thin plates and surface reconstruction can be excluded as only very weak additional diffractions can be observed in these two cases. In the stacking faults model, the intensity of the 1/3{422} reflections depends on the number of the stacking faults, the different stacking sequences and the thickness of the samples. In Fig. 2(b), the ultra-intense forbidden 1/3{422} reflections indicate the presence of high-density stacking faults and micro twin structures along the <111> direction of the fcc structure. Therefore, the imperfect ABCABC... packing causes a transition from the fcc crystal cell to a hexagonal crystal cell, and the as-prepared hexagram particles can be considered as a quasi-hexagonal crystal structure. It should be pointed out that the appearance of hexagonal symmetry is not normally observed for a crystal with the fcc structure. The presence of high-density stacking faults along the <111> direction of the fcc structure, resulting in a quasi-hexagonal crystal structure, could be the reason for the formation of the Au hexagram particles.
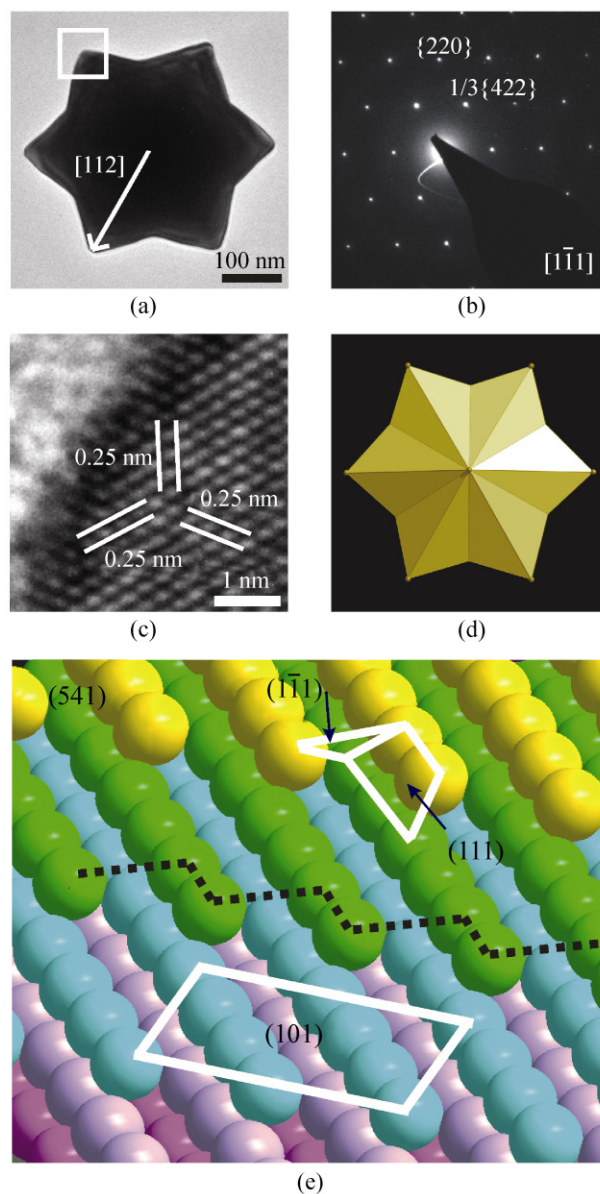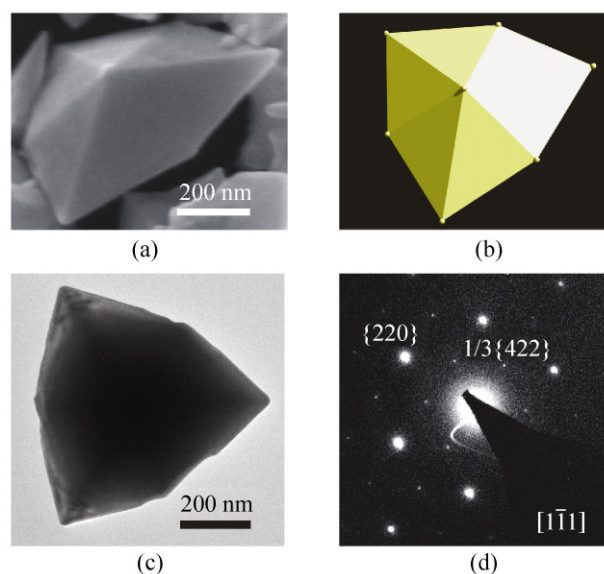

Figure 2 (a) Low magnification TEM image of a typical NC, recorded along the [1$\bar{1}$1] direction. (b) The corresponding SAED pattern taken from the [1$\bar{1}$1] direction. (c) HRTEM image of the NC recorded from the square enclosed regions in (a). (d) Model of an ideal hexagram viewed from the [1$\bar{1}$1] direction overlapped on the image in (a). (e) Atomic model of the Au (541) surface

Combining the morphology information from the SEM images and the crystal information from the TEM images and related indexed diffraction patterns, a schematic model of the hexagram can be constructed, because when the orientation of a single crystal is fixed, the morphology is determined by the exposed crystal planes, and vice versa. In the present case, the hexagonal star enclosed by {541} surfaces has been

found to match perfectly to the geometric information obtained from the SEM and TEM images, as shown in Fig. 2(d) and Figs. S-2 and S-3 (in the ESM). Based on these results, the surface of the hexagram shaped Au particles can be concluded to be high index {541} and its vicinal high index crystal planes. An atomic model of the Au (541) surface is shown in Fig. 2(e). Different from the reported metal NCs enclosed by high index facets with steps (the {hhl} or {hk0} facets), kinks are present on the Au (541) surface as shown by a black zigzag dashed line in Fig. 2(e). In fact, the high index planes can be described as the combination of some low index planes. For example, the microstructure of a (541) facet can be thought of as the combination of (101) terraces, (111) and $(1\bar{1}1)$ steps as shown in Fig. 2(e), where the solid frames show the Miller indices of the terrace and steps. It can be seen that the kinks exist in the junctions among the (101) terraces, and the two equivalent (111) steps, as shown in Fig. 2(e) (a close up view of the step edge).

By investigating the SEM images carefully, another kind of well-defined hexagonal shaped particles can be found in our product, as shown in Fig. 3(a). Statistical results showed that about 5% of the synthesized Au crystals exhibited a hexagonal shield shape with the regular three-fold symmetry of an fcc metal. Such a hexagonal shield can be thought as the analogue of the hexagram, obtained by cutting off three horns. Figure 3(b) shows a geometrical model of a hexagonal shield enclosed by 12 {541} surfaces. The proposed model agrees well with the morphology of the as-prepared hexagonal shields. Figure 3(c) shows a typical TEM image of an individual hexagonal shield. The corresponding SAED patterns (Fig. 3(d)) also show regular hexagonal diffraction spot arrays, which are similar to that of the hexagram shaped gold particles. However, the closest strong reflections to the direct beam are six allowed {220} Bragg reflections. The 1/3{422} reflections are very weak, indicating only a few stacking faults are present in the hexagonal shields.

It is worthwhile to note that, although there are particles with irregular star-shape present in our product, careful SEM observations indicated that they are formed by deformation of regular hexagram shaped particles. Figure 4 shows SEM images of some of these branched particles. Although the particles were

Figure 3 (a) High-magnification SEM image of a single hexagonal shield shaped Au NC. (b) Schematic illustration of an ideal hexagonal shield enclosed by {541} surfaces in the same orientation as the NCs in the SEM image. (c) TEM image and (d) the corresponding SAED pattern of a typical hexagonal shield NC, recorded along the $[1\bar{1}1]$ direction
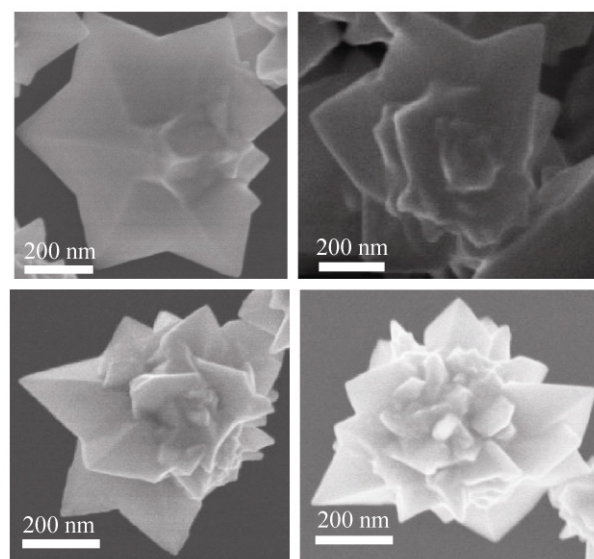
Figure 4 SEM images of various irregular gold particles in the products

branched in different ways, every single branch has very similar shape to the regular hexagram particles. This suggests that the star shaped particles are analogues of the hexagram particles, which was confirmed by the surface sensitive electrochemical experiments (discussed in the next section).

3.2 Electrochemical characterization

In order to further study the surface structures of all the prepared NCs in our product, surface structure sensitive electrochemical reactions were carried out. The normal CV traces of various gold electrodes in H$_2$SO$_4$ can give important surface structure information. Different characteristic peaks in the surface oxide formation region correspond to different site symmetries. Clearly, the electrochemical behavior of the hexagram shaped NCs (as shown in Fig. 5, dotted line) was different from that of a polycrystalline gold electrode (Fig. 5, dash line), and also different from that of the {111}, {110}, and {100} surfaces of a gold single crystal [37]. In addition, only {110} and {111} sites contribute to the CV peaks of the gold NCs having exposed {541} facets as shown in Fig. 5. This result suggests that the as-prepared well-faceted Au NCs are neither enclosed by low index surfaces nor by a polycrystalline surface, but by surfaces formed by a combination of {110} sites and {111} sites.

For the purpose of verifying the surface structure, UPD of Pb in alkaline media was carried out (Fig. 6), as it can give rise to several characteristic peaks on the voltammetric profile for different surface structures [38, 39]. For comparison, we prepared Au octahedral (Fig. S-4 in the ESM) and Au truncated cubic particles as a reference. Au octahedral particles are enclosed by eight (111) facets. The CVs of Au octahedral particles give a very sharp peak oxidation peak at about 0.435 V
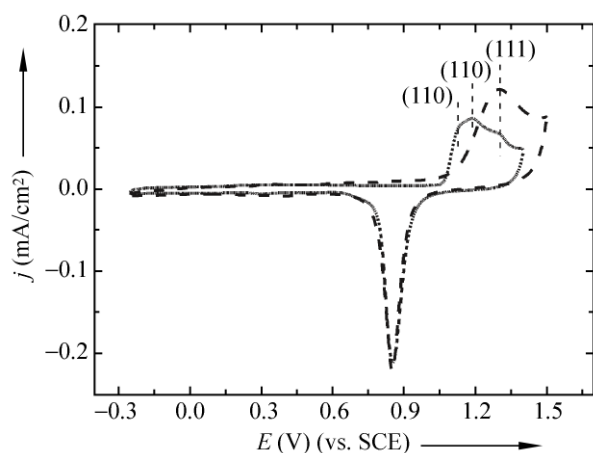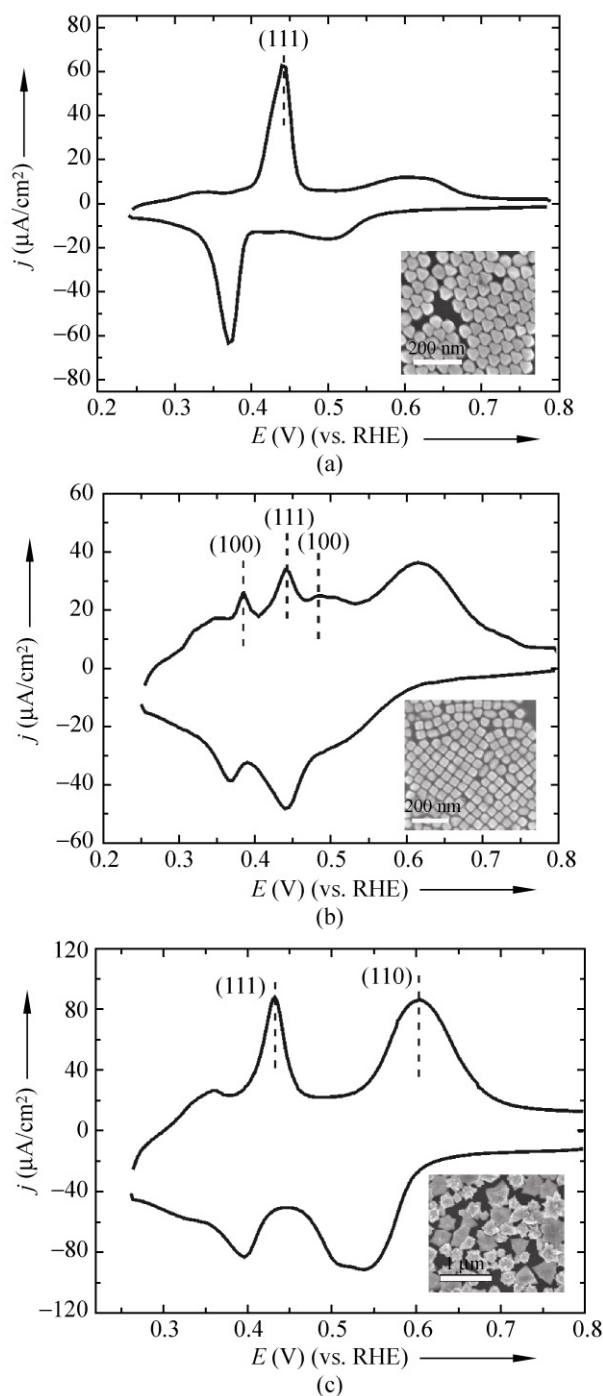

Figure 5 Current–potential curves of a polycrystalline Au electrode (dash line) and the Au NCs with exposed {541} facets (dotted line) in 0.1 mol/L H$_2$SO$_4$. Scan rate: 50 mV/s

(vs. the reference hydrogen electrode (RHE)) (Fig. 6(a)), which corresponds well to the stripping of the Pb UPD layer from Au {111} surfaces [38]. For our Au truncated cube particles, two sharp oxidation peaks were observed at about 0.385 V (vs. RHE) and 0.435 V (vs. RHE), corresponding to contributions from the {100} and {111} facets. For the truncated cube particles, the {111} and {100} facets coexist on the particle surface, and therefore both peaks appear (Fig. 6(b)). Meanwhile, a broader peak appears at about 0.61 V (vs. RHE), which could be the influence of sites on the edge, mainly consisting of the (110) surface. It should be noted that better shaped cube nanoparticles exhibited a stronger (100) peak, as can be seen in Ref. [39]. For the case of as-prepared Au NCs having exposed {541} facets, as shown in Fig. 6(c), two main sharp peaks are observed in the oxidative dissolution profile of Pb. The first one at 0.435 V (vs. RHE) corresponds to the contribution of the (111) sites, the second one at 0.608 V (vs. RHE) is related to the presence of the (110) terraces. No contribution from the (100) sites can be observed. This result further confirms that the surfaces are a combination of the (111) and (110) sites, which is consistent with the atomic model of Au (541) as shown in Fig. 2(e).

3.3 Formation mechanism

Solution-based methods are widely used for the preparation of noble metal NCs. In most cases, so-called capping agents (usually surfactants) are introduced to guide the growth of specific facets and prevent aggregation of the NCs. Cetyltrimethylammonium bromide (CTAB) is a well-known surfactant for the preparation of Au NCs, in which the exposed surfaces are usually low index facets, such as cubes with {100} facets [20], plates with {111} facets [40] and rods with {100} facets as side surfaces [41, 42]. These results implied that the adsorption of bromide ions in combination with cetyltrimethylammonium ions may stabilize {100} or {111} facets. When cetyltrimethylammonium chloride (CTAC) was used to substitute the CTAB under appropriate experimental conditions (AA as the reductant), trisoctahedral Au NCs with high index {221} facets were obtained [25]. Instead of a flat terrace, the {221} facets have steps, which consist of (111) terraces and (110) steps. The results indicate that

Figure 6 Current–potential curves of (a) Au octahedra, (b) truncated Au cubes and (c) as-prepared Au NCs in 0.1 mol/L NaOH + 10^{-3} mol/L Pb(NO$_3$)$_2$. Scan rate: 20 mV/s. Insets are the corresponding SEM images of the Au particles

(110) steps can be stabilized in the absence of bromide ions, which implies that bromide ions favor the (100) and (111) surface sites. As the specific adsorption ability of bromide ions is much stronger than that of chloride

ions, the absence of bromide ions thus greatly affects the surface energy of the (100) and (111) surfaces, and as result (110) steps appear on the surface. According to this hypothesis, we added PDDA (a relatively new surfactant containing chloride anions) to the solution in order to further tune the surface structure of the Au crystals, and we successfully obtained hexagram shaped Au NCs with high index {541} facets. Compared with the trioctahedral Au NCs with {221} facets formed by using CTAC as the surfactant, the surface of the hexagram shaped Au NCs formed under the protection of PDDA consists of {110} terraces, {111} steps and kinks. This result indicates that the surface structure can be fine tuned by selection of the capping agent, although the detailed factors influencing the surface energy of various crystal facets are still unknown.

PDDA is a type of cationic polymer. PDDA may form stable ion pairs with AuCl$_4^-$ through electrostatic interactions. In addition PDDA can adsorb on the Au crystal surfaces, which should modify their surface energies, leading to the formation of NCs with specific facets. Energy dispersive X-Ray spectroscopy (EDS) and Raman spectra collected directly from the washed sample showed that PDDA cations together with Cl$^-$ ions were strongly adsorbed on the surface of the Au hexagrams and their analogues (see Fig. S-5 in the ESM). Polyvinylpyrrolidone (PVP) is a neutral polymer. When PVP was used as a substitute for PDDA under appropriate experimental conditions (AA as the reductant), star-shaped Au plates with exposed {111} facets were obtained [43]. Therefore, co-adsorption of PDDA and Cl$^-$ ions on the gold surfaces plays a key role in the formation of Au hexagrams and their analogues, especially in the formation of the {541} facets.

It is well known that surface energies are associated with different Au crystallographic facets and increase in the order {111} < {100} < {110} < {hkl}. The capping effect of PDDA on the {541} facets reduces the surface energy of {541} under our experimental conditions, resulting in the formation of hexagram shaped Au particles with {541} facets. It should be noted that our experiments were carried out at a relatively low temperature. Increasing the temperature usually weakens the adsorption of a chemical species, especially for the case of physisorption. Therefore, at high temperatures, the surface energy of the (111) surface may still be the

lowest even in the presence of PDDA. It has been reported that Au octahedra [44] and Au plates [45], with exposed {111} facets, were obtained using PDDA at high temperatures. A similar phenomenon was observed in our reaction system. For example, when the reaction temperature was increased to 120 ℃, the products were decahedral and plate-like Au particles having only exposed {111} facets; no hexagram gold particles were observed (see Fig. S-6 in the ESM).

3.4   Electrocatalytic performance

Fundamental studies of single-crystal surfaces of bulk metals have showed that high index facets having a high density of atomic steps, ledges, kinks, and dangling bonds usually exhibit higher chemical activities [18, 19]. It has been reported that metal polyhedra enclosed by high index facets ({hk0} or {hhl}) have relatively high electrocatalytic activities [23–28, 30]. This suggests that the hexagram shaped Au particles and their analogues with exposed {541} facets may have high electrocatalytic activities owing to the open surface structure with a high density of kink atoms.

   The structure–functionality relationship was therefore studied by employing electrocatalytic oxidation of AA as a probe reaction. The electroactive surface area of Au NC working electrodes were determined from the charge for the reduction of the Au surface oxide monolayer using the reported value of 400 μC/cm^2 for a cleaned Au electrode [27, 46, 47]. It should be emphasized here that when evaluating the electroactive surface area from the reduction of the Au surface oxide monolayer, attention should be paid to the potential up-limit value, avoiding the over-oxidation of gold. Figure 7 shows current–potential curves of AA oxidation on three kinds of gold NPs—the as-prepared hexagram gold particles (green line), the gold cubes with exposed {100} facets (red line) [20] and the gold trioctahedra with exposed {221} facets (blue line) [25] (SEM images and XRD data for these materials are given in Figs. S-7 and S-8 in the ESM). The peak current of Au {541} was 1.8 times that for Au {221} and 4.25 times that for Au {100}, as shown in Fig. 7. The onset potential of AA oxidation on as-prepared hexagram Au particles was negatively shifted by about 50 mV in comparison with that on the cubic and trioctahedral Au
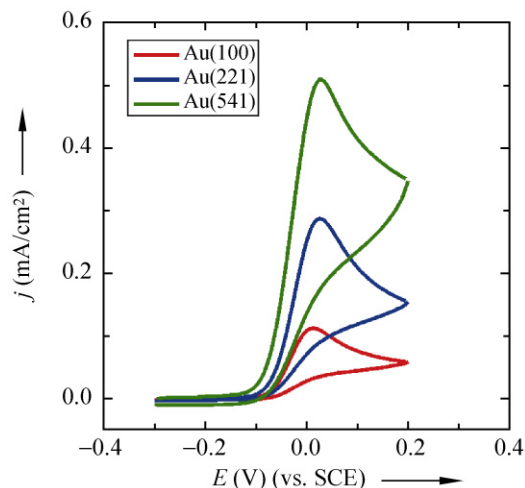
Figure 7   Current–potential curves of electrooxidation of 10 mmol/L AA in 0.1 mol/L phosphate buffered solution (PBS). scan rate: 50 mV/s

particles. This confirms that the as-prepared hexagram particles having kinks and steps exhibit the highest electrocatalytic activity of the three kinds of Au particles. Au trioctahedral particles having only steps exhibit lower electrocatalytic activity, and the Au cubes having only low index {100} terraces exhibit the lowest electrocatalytic activity. The high peak current and the significantly negative shift of the onset potential for AA oxidation on hexagram shaped Au NCs are due to the low activation energy on the surfaces of Au {541}, which should be correlated with the high density of kink atoms on such high index facets.

4. Conclusions

Hexagram shaped polyhedral Au particles have been successfully synthesized by reducing HAuCl$_4$ with AA in the presence of PDDA at room temperature. SEM and TEM observations suggested that the as-prepared Au hexagram particles are enclosed by 24 high index facets with kinks, such as {541} planes. Other particles are analogues of the Au hexagrams, having similar high index facets on their surfaces. Surface structure sensitive electrochemical studies showed that the as-prepared NCs have an electrochemical behavior different from that of low index surfaces of a single crystal of Au and from that of a surface of polycrystalline Au. The hexagram shaped Au NCs exhibit a

very high activity in AA electrocatalytic oxidation, attributed to their high index facets that provide a high density of step atoms and especially the kink atoms. Considering the unique surface structure, hexagram shaped gold NCs and their analogues should be important for both theoretical investigations and practical applications, such as catalysis and surface-enhanced Raman spectroscopy (SERS). The present study also motivates us to further explore methods for the preparation of other well-defined polyhedral metal NCs enclosed by high index facets.

Acknowledgements

Electronic Supplementary Material: SEM images and corresponding proposed models in the same orientation, TEM data and ideal hexagrams overlapped on the TEM images viewed from different directions, deformations of the hexagram shaped gold particles during crystal growth, HRTEM images recorded from different parts of the hexagram gold crystals, SEM images and TEM image of Au octahedra, EDS and Raman spectra collected from the washed Au sample, SEM images of Au particles obtained at 120 ℃, SEM images of gold trioctahedra and cubes, and X-ray diffraction patterns of Au hexagrams, Au trisoctahedra and Au cubes are available in the online version of this article at http://dx.doi.org/10.1007/s12274-011-0117-x.

References

[1]   Somorjai, G. A.; Blakely, D. W. Mechanism of catalysis of hydrocarbon reactions by platinum surfaces. *Nature* **1975**, *258*, 580–583.

[2]   Somorjai, G. A. Modern surface science and surface technologies: An introduction. *Chem. Rev.* **1996**, *96*, 1223–1236.

[3]   Baldauf, M.; Kolb, D. M. Formic acid oxidation on ultrathin Pd films on Au(*hkl*) and Pt(*hkl*) electrodes. *J. Phys. Chem.* **1996**, *100*, 11375–11381.

[4]   Hoshi, N.; Kida, K.; Nakamura, M.; Nakada, M.; Osada, K. Structural effects of electrochemical oxidation of formic acid on single crystal electrodes of palladium. *J. Phys. Chem. B* **2006**, *110*, 12480–12484.

[5]   Mahmoud, M. A.; Tabor, C. E.; El-Sayed, M. A.; Ding, Y.; Wang, Z. L. A new catalytically active colloidal platinum nanocatalyst: The multiarmed nanostar single crystal. *J. Am. Chem. Soc.* **2008**, *130*, 4590–4591.

[6]   Lee, H.; Habas, S. E.; Kweskin S.; Butcher D.; Somorjai, G. A.; Yang, P. D. Morphological control of catalytically active platinum nanocrystals. *Angew. Chem. Int. Ed.* **2006**, *45*, 7824–7828.

[7]   Narayanan, R.; El-Sayed, M. A. Catalysis with transition metal nanoparticles in colloidal solution: Nanoparticle shape dependence and stability. *J. Phys. Chem. B* **2005**, *109*, 12663–12676.

[8]   Zijlstra, P.; Chon, J. W. M.; Gu, M. Five-dimensional optical recording mediated by surface plasmons in gold nanorods. *Nature* **2009**, *459*, 410–413.

[9]   Tao, A. R.; Habas, S.; Yang, P. D. Shape control of colloidal metal nanocrystals. *Small* **2008**, *4*, 310–325.

[10] Tian, Z. Q.; Ren, B.; Wu, D. Y. Surface-enhanced Raman scattering: From noble to transition metals and from rough surfaces to ordered nanostructures. *J. Phys. Chem. B* **2002**, *106*, 9463–9483.

[11] Choi, J. S.; Choi, H. J.; Jung, D. C.; Lee, J. H.; Cheon, J. Nanoparticle assisted magnetic resonance imaging of the early reversible stages of amyloid β self-assembly. *Chem. Commun.* **2008**, 2197–2199.

[12] Meulenberg, R. W.; Lee, J. R. I.; McCall, S. K.; Hanif, K. M.; Haskel, D.; Lang, J. C.; Terminello, L. J.; Buuren, T. V. Evidence for ligand-induced paramagnetism in CdSe quantum dots. *J. Am. Chem. Soc.* **2009**, *131*, 6888–6889.

[13] Boisselier, E.; Astruc, D. Gold nanoparticles in nanomedicine: Preparations, imaging, diagnostics, therapies and toxicity. *Chem. Soc. Rev.* **2009**, *38*, 1759–1782.

[14] Yang, H. G.; Sun, C. H.; Qiao, S. Z.; Zou, J.; Liu, G.; Smith, S. C.; Cheng, H. M.; Lu, G. Q. Anatase TiO₂ single crystals with a large percentage of reactive facets. *Nature* **2008**, *453*, 638–641.

[15] Hang, X. G.; Kuang, Q.; Jin, M. S.; Xie, Z. X.; Zheng, L. S. Synthesis of titania nanosheets with a high percentage of exposed (001) facets and related photocatalytic properties. *J. Am. Chem. Soc.* **2009**, *131*, 3152–3153.

[16] Yang, H. G.; Liu, G.; Qiao, S. Z.; Sun, C. H.; Jin, Y. G.; Smith, S. C.; Zou, J.; Cheng, H. M.; Lu, G. Q. Solvothermal synthesis and photoreactivity of anatase TiO₂ nanosheets with dominant {001} facets. *J. Am. Chem. Soc.* **2009**, *131*,

4078–4083.

[17] Xie, X. W.; Li, Y.; Liu, Z. Q.; Haruta, M.; Shen, W. J. Low-temperature oxidation of CO catalysed by Co₃O₄ nanorods. *Nature* **2009**, *458*, 746–749.

[18] Lebedeva, N. P.; Koper, M. T. M.; Feliu, J. M.; van Santen, R. A. Role of crystalline defects in electrocatalysis: Mechanism and kinetics of CO adlayer oxidation on stepped platinum electrodes. *J. Phys. Chem. B* **2002**, *106*, 12938–12947.

[19] Sun, S. G.; Chen, A. C.; Huang, T. S.; Li, J. B.; Tian, Z. W. Electrocatalytic properties of Pt(111), Pt(332), Pt(331) and Pt(110) single crystal electrodes towards ethylene glycol oxidation in sulphuric acid solutions. *J. Electroanal. Chem.* **1992**, *340*, 213–216.

[20] Sau, T. K.; Murphy, C. J. Room temperature, high-yield synthesis of multiple shapes of gold nanoparticles in aqueous solution. *J. Am. Chem. Soc.* **2004**, *126*, 8648–8649.

[21] Li, C. C.; Shuford, K. L.; Park, Q. -H.; Cai, W. P.; Li, Y.; Lee, E. J.; Cho, S. O. High-yield synthesis of single-crystalline gold nano-octahedra. *Angew. Chem. Int. Ed.* **2007**, *46*, 3264–3268.

[22] Niu, W. X.; Zheng, S. L.; Wang, D. W.; Liu, X. Q.; Li, H. J.; Han, S.; Chen, J. A.; Tang, Z. Y.; Xu, G. B. Selective synthesis of single-crystalline rhombic dodecahedral, octahedral, and cubic gold nanocrystals. *J. Am. Chem. Soc.* **2009**, *131*, 697–703.

[23] Tian, N.; Zhou, Z. Y.; Sun, S. G.; Ding, Y.; Wang, Z. L. Synthesis of tetrahexahedral platinum nanocrystals with high-index facets and high electro-oxidation activity. *Science* **2007**, *316*, 732–735.

[24] Tian, N.; Zhou, Z. Y.; Sun, S. G. Platinum metal catalysts of high-index surfaces: From single-crystal planes to electrochemically shape-controlled nanoparticles. *J. Phys. Chem. C* **2008**, *112*, 19801–19817.

[25] Ma, Y. Y.; Kuang, Q.; Jiang, Z. Y.; Xie, Z. X.; Huang, R. B.; Zheng, L. S. Synthesis of trisoctahedral gold nanocrystals with exposed high-index facets by a facile chemical method. *Angew. Chem. Int. Ed.* **2008**, *47*, 8901–8904.

[26] Ming, T.; Feng, W.; Tang, Q.; Wang, F.; Sun, L. D.; Wang, J. F.; Yan, C. H. Growth of tetrahexahedral gold nanocrystals with high-index facets. *J. Am. Chem. Soc.* **2009**, *131*, 16350–16351.

[27] Liao, H. G.; Jiang, Y. X.; Zhou, Z. Y.; Chen, S. P.; Sun, S. G. Shape-controlled synthesis of gold nanoparticles in deep eutectic solvents for studies of structure–functionality relationships in electrocatalysis. *Angew. Chem. Int. Ed.* **2008**, *47*, 9100–9103.

[28] Zhang, J.; Langille, M. R.; Personick, M. L.; Zhang, K.; Li, S. Y.; Mirkin, C. A. Concave cubic gold nanocrystals with high-index facets. *J. Am. Chem. Soc.* **2010**, *132*, 14012–14014.

[29] Yu, Y.; Zhang, Q. B.; Lu, X. M.; Lee, J. Y. Seed-mediated synthesis of monodisperse concave trisoctahedral gold nanocrystals with controllable sizes. *J. Phys. Chem. C* **2010**, *114*, 11119–11126.

[30] Li, J.; Wang, L. H.; Liu, L.; Guo, L.; Han, X. D.; Zhang, Z. Synthesis of tetrahexahedral Au nanocrystals with exposed high-index surfaces. *Chem. Commun.* **2010**, *46*, 5109–5111.

[31] Kim, D. Y.; Im, S. H.; Park, O. O. Synthesis of tetrahexahedral gold nanocrystals with high-index facets. *Cryst. Growth Des.* **2010**, *10*, 3321–3323.

[32] Murphy, C. J.; Sau, T. K.; Gole, A. M.; Orendorff, C. J.; Gao, J. X.; Gou, L. F.; Hunyadi, S. E.; Li, T. Anisotropic metal nanoparticles: Synthesis, assembly, and optical applications. *J. Phys. Chem. B* **2005**, *109*, 13857–13870.

[33] Liang, H. Y.; Yang, H. X.; Wang, W. Z.; Li, J. Q.; Xu, H. X. High-yield uniform synthesis and microstructure-determination of rice-shaped silver nanocrystals. *J. Am. Chem. Soc.* **2009**, *131*, 6068–6069.

[34] Germain, V.; Li, J.; Ingert, D.; Wang, Z. L.; Pileni, M. P. Stacking faults in formation of silver nanodisks. *J. Phys. Chem. B* **2003**, *107*, 8717–8720.

[35] Zhang, S. H.; Jiang, Z. Y.; Xie, Z. X.; Xu, X.; Huang, R. B.; Zheng L. S. Growth of silver nanowires from solutions: A cyclic penta-twinned-crystal growth mechanism. *J. Phys. Chem. B* **2005**, *109*, 9416–9421.

[36] Aherne, D.; Ledwith, D. M.; Gara, M.; Kelly, J. M. Optical properties and growth aspects of silver nanoprisms produced by a highly reproducible and rapid synthesis at room temperature. *Adv. Funct. Mater.* **2008**, *18*, 2005–2016.

[37] Hamelin, A. Cyclic voltammetry at gold single-crystal surfaces. Part 1. Behaviour at low-index faces. *J. Electroanal. Chem.* **1996**, *407*, 1–11.

[38] Hernández, J.; Solla-Gullón, J.; Herrero, E. Gold nanoparticles synthesized in a water-in-oil microemulsion: Electrochemical characterization and effect of the surface structure on the oxygen reduction reaction. *J. Electroanal. Chem.* **2004**, *574*, 185–196.

[39] Hernández, J.; Solla-Gullón, J.; Herrero, E.; Aldaz, A.; Feliu, J. M. Electrochemistry of shape-controlled catalysts: Oxygen reduction reaction on cubic gold nanoparticles. *J. Phys. Chem. C* **2007**, *111*, 14078–14083.

[40] Wang, Z. J.; Yuan, J. H.; Zhou, M.; Niu, L.; Ivaska, A. Synthesis, characterization and mechanism of cetyltrimethylammonium bromide bilayer-encapsulated gold nanosheets and nanocrystals. *Appl. Surf. Sci.* **2008**, *254*, 6289–6293.

[41] Kou, X. S.; Zhang, S. Z.; Tsung, C. K.; Yang, Z.; Yeung, M. H.; Stucky, G. D.; Sun, L. D.; Wang, J. F.; Yan, C. H. One-step synthesis of large-aspect-ratio single-crystalline gold nanorods by using CTPAB and CTBAB surfactants. *Chem. Eur. J.* **2007**, *13*, 2929–2936.

[42] Gole, A.; Murphy, C. J. Seed-mediated synthesis of gold nanorods: Role of the size and nature of the seed. *Chem. Mater.* **2004**, *16*, 3633–3640.

[43] Yamamoto, M.; Kashiwagi, Y.; Sakata, T.; Mori, H.; Nakamoto, M. Synthesis and morphology of star-shaped gold nanoplates protected by poly(*N*-vinyl-2-pyrrolidone). *Chem. Mater.* **2005**, *17*, 5391–5393.

[44] Li, C. C.; Shuford, K. L.; Chen, M. H.; Lee, E. J.; Cho, S. O. A facile polyol route to uniform gold octahedra with tailorable size and their optical properties. *ACS Nano* **2008**, *2*, 1760–1769.

[45] Chen, H. J.; Wang, Y. L.; Dong, S. J. An effective hydrothermal route for the synthesis of multiple PDDA-protected noble-metal nanostructures. *Inorg. Chem.* **2007**, *46*, 10587–10593.

[46] Trasatti, S.; Petrii, O. A. Real surface area measurements in electrochemistry. *Pure Appl. Chem.* **1991**, *63*, 711–734.

[47] Woods, R. Chemisorption at electrodes: Hydrogen and oxygen on nobel metals and their alloys. In *Electroanalytical Chemistry–A Series of Advances*; Bard, A. J., Ed.; Marcel Dekker, Inc.: New York and Basel, 1976; pp. 119–125.